KSCE Journal of Civil Engineering (2019) 23(3):1132-1140

DOI 10.1007/s12205-019-1519-7

Hydraulic Engineering

pISSN 1226-7988, eISSN 1976-3808
www.springer.com/12205

Experimental Study on Seepage and Stress of Single-fracture Radiation Flow

Xin Zhang*, Junrui Chai, Yuan Qin***, Jing Cao****, and Cheng Cao*******

Received July 30, 2018/Revised September 19, 2018/Accepted November 4, 2018/Published Online January 14, 2019

Abstract

Studying the stress distribution and water flow law of rocks under stress and seepage pressure in different directions can provide a certain basis for rock stability. In this experiment, a test system instrument for coupling direct shear and seepage of rock joints was developed to analyze the fracture seepage and shear stress of the relatively smooth surface formed by gypsum specimens. The seepage considered in this study refers to the groundwater at a depth of 80–150 m below the surface. Moreover, a radiation flow model was established, and a new law was obtained by fitting the relationship between flow rate and mechanical aperture. The shear process was divided into three phases. Normal stress and contact surface undulation had a considerable influence on shear stress. A two-dimensional numerical model showed that the vortices were the important cause of damage to the radiation flow. Increasing the seepage pressure increased the flow velocity between the fractures. The maximum flow velocity on one side of the same shear direction was larger than that on the other side.

Keywords: *single fracture, radiation flow, seepage, shear stress, mechanical aperture*

1. Introduction

When water flows in high-permeability media, it is diffused by the flow path of fractures (Chai and Xu, 2011). Therefore, studying the seepage characteristics of fluids from the perspective of fracture elements is of considerable importance (Zhang *et al.*, 2016). The main applicability for studying these characteristics is dam foundation stability (Yun *et al.*, 2013), seam grouting, groundwater utilization, and sewage treatment of landfill waste. When fluid comes in contact with solids, the roughness of the solid surface, the boundary stress and the physical properties of the fluid affect the fluid flow (Xia *et al.*, 2016). Therefore, investigating the fluid–solid coupling problem of single-fracture fluid is particularly important (Nguyen-Thoi *et al.*, 2015).

Cubic law, which is the basic law of single-fracture seepage, proposes that the seepage flow and the fracture width are in a cubic relationship between ideal smooth parallel plates (Witherspoon *et al.*, 1979). In practice, however, the roughness of the fracture surface and cross phenomenon can affect the velocity distribution of water flow. Meanwhile, the non-linear flow in different contact forms can change the solid boundary stress, heat transfer distribution, and the seepage flow velocity (Seo *et al.*, 2017; Bai *et al.*, 2017).

The fracture distribution of a rough fracture surface belongs to a discrete network (Jeong *et al.*, 2001), and the permeability varies substantially at different positions of the same single fracture (Jin *et al.*, 2017; Qian *et al.*, 2005). Many scholars have established a series of correction equations for the seepage relationship among rough fractures (He *et al.*, 2016). In the fracture of granite with a low-permeability coefficient, the Reynolds number (*Re*) can describe the pattern of water flow and establish the power relations of seepage flow with hydraulic fracture width, hydraulic gradient, and surface roughness (Oda *et al.*, 2002; Rong *et al.*, 2017). Three-dimensional (3D) and two-dimensional (2D) models are established under a certain fracture width, and the calculated flow error is approximately 12%–15% (Li *et al.*, 2016; Liu *et al.*, 2016).

The coupling of seepage and stress has been a constant and crucial topic (Develi and Babadagli, 2015; Giwelli *et al.*, 2014; Tang *et al.*, 2016). The critical *Re* is related not only to the

*M.Sc. Student, State Key Laboratory of Eco-hydraulics in Northwest Arid Region of China, Xi'an University of Technology, Xi'an 710048, China (E-mail: 764689881@qq.com)

**Professor, State Key Laboratory of Eco-hydraulics in Northwest Arid Region of China, Xi'an University of Technology, Xi'an 710048, China; School of Civil Engineering, Xijing University, Xi'an 710123, China (E-mail: jrchai@xaut.edu.cn)

***Associate Professor, State Key Laboratory of Eco-hydraulics in Northwest Arid Region of China, Xi'an University of Technology, Xi'an 710048, China (Corresponding Author, E-mail: lanelyly@163.com)

****Lecturer, State Key Laboratory of Eco-hydraulics in Northwest Arid Region of China, Xi'an University of Technology, Xi'an 710048, China (E-mail: caojingxn@163.com)

*****M.Sc. Student, State Key Laboratory of Eco-hydraulics in Northwest Arid Region of China, Xi'an University of Technology, Xi'an 710048, China (E-mail: caocheng_xaut@163.com)

surface roughness but also to normal and shear forces. The most typical theory is that of Newtonian fluid (McClure and Kang, 2017). When two parallel plates move at a relative speed, the shear stress velocity of the water flow between two plates is linearly distributed. When the plates are tilted or when impurities exist in the water flow, the current becomes a non-Newtonian flow (Chamkha *et al.*, 2015; Dogonchi *et al.*, 2015; Subbarao *et al.*, 2016). When normal force is applied, the destruction of the single-fracture surface results in hydraulic fracturing (Xu *et al.*, 2017). After the fracture surface is destroyed, debris is formed, which is prone to pulse phenomenon. The fracture water flow becomes a solute transport problem, which is also an inevitable research direction of single-fracture seepage. Shear stress is likely to cause fracture distribution and water flow conditions (Zou *et al.*, 2017). Eddies exist in the local area, *Re* increases sharply, and water flow is turbulent (Adrian, 2006). In summary, the fluid flow state and stress changes of a single fracture are interactional and inseparable.

Horizontal flow is the most common form of water flow, and the flow rule is relatively simple. Radiation flow is used extensively in magnetic fluid mechanics. In porous media, the occurrence of convection and radiation flow in 2D fluid has been reported, and the theory is comprehensive (El-Hakiem, 2000; Raptis, 1998; Sheikholeslami *et al.*, 2015). Energy and momentum losses occur in the convection of infinite parallel porous plates, and the entropy changes, which is consistent with the behavior of Newtonian and non-Newtonian fluids (Ma *et al.*, 2018; Rashidi *et al.*, 2015). Normal water flow is introduced into the fracture with a certain amount of seepage pressure, and its velocity satisfies the linear relationship under the minimum hydraulic gradient. Furthermore, instability remains at a large hydraulic gradient (Zhao *et al.*, 2017).

In this study, experimental and numerical simulation methods are selected to study the seepage problem of single-fracture radiation flow. First, the radiation flow process is analyzed. Second, the relationship between fracture width and flow rate is discussed on the basis of the experimental results. Then, cubic law is modified. Finally, the velocity distribution of radiation flow in the shear process is studied numerically.

2. Radiation Flow Analysis

Water flow between single fractures satisfies the basic laws of fluid dynamics. Navier–Stokes (N–S) equations (Kang and Sotiropoulos, 2015) conform to the motion of incompressible fluid between fractures. However, in the case of relatively smooth fractures, the water flow satisfies cubic law to simplify the calculation. The smooth parallel plate model is the basic model for studying the seepage of a single fracture. Two smooth, straight, and infinitely long parallel plates are assumed to exist on the basis of cubic law, and the fracture fluid is incompressible laminar fluid. Cubic law is derived as follows (Witherspoon *et al.*, 1979):

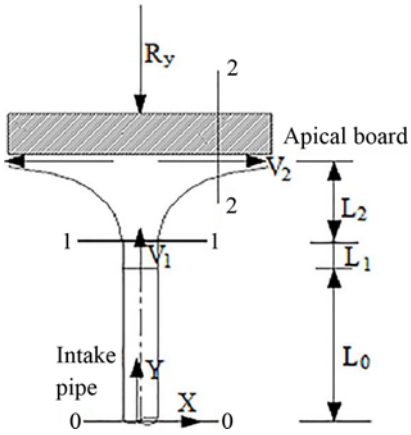

Fig. 1. Radiation Flow Diagram

$$q = \frac{gb^3}{12\nu}J, \tag{1}$$

where q is the flow rate, g is the gravitational acceleration, ν is the dynamic viscosity, b is the fracture width, and J is the hydraulic gradient.

Figure 1 shows a 2D radiation flow model. The water flow is directed normally toward the upper plate through the inlet pipe. The upper plate is assumed to be absolutely smooth, and the water flow is incompressible. The flow rates are equal in all directions along the plate surface. Table 1 compares the four differences of radiation flow and parallel plate water flow in the inlet direction, flow expansion, flow process, and time consumption.

When the water flow inlet velocity (v_0), inlet pressure (p_1), and inlet area (A) are determined, the water flows freely out on the plate. Section 0–0 is selected as the reference plane, and the isolator for sections 1–1 and 2–2 is taken. The momentum equation in the Y direction is established. The seepage flow (q), gravity (G), and plate force (Ry) on the flow are selected for force analysis. The momentum equation is established as follows (Coimbra and Rangel, 2002):

$$p_1 \cdot A - 0 - G - R_y = \rho \cdot q \cdot (\beta_2 \cdot V_{2y} - \beta_1 \cdot V_{1y}). \tag{2}$$

Table 1. Differences between Parallel Plate Flow and Radiation Flow

Differences	Parallel plate water flow	Radiation flow
Direction of water inlet	Flow in horizontally	Flow in vertically
Flow expansion	Rectangle	Circle
Flow process	Laminar flow all the time	Turbulence occurs in radiant water
Time	Short	Long (Energy loss is determined at the radiant stream.)

Moreover,

$$q = v_0 \cdot A\,; \tag{2a}$$

$$G = m \cdot g = \rho \cdot q \cdot g = \rho \cdot v_0 \cdot A \cdot g; \tag{2b}$$

$$\frac{1}{2}m \cdot V_1^2 - \frac{1}{2}m \cdot V_0^2 = m \cdot g \cdot L_0; \tag{2c}$$

$$v_1 = \sqrt{2gL_0 + V_0^2}\,. \tag{2d}$$

The simplified form is as follows:

$$R_y = A \cdot [p_1 - \rho \cdot v_0 \cdot (g - \beta_1 \cdot \sqrt{2g \cdot L_0 + v_0^2})]\,. \tag{3}$$

The magnitude of the external force (R_y) of the water flow on the parallel plate can be calculated, and the direction is upward. (β_1 is the momentum correction factor for section 1–1.)

For comparison with the parallel plate law, the upper plate is assumed to be smooth; thus, the water flow in the inlet pipe and among the plates is laminar, and the frictional head loss (h_f) exists only in the circular pipe. A local head loss (h_j) is determined in the local range of water flow radiation on the plate. The energy equation is accordingly established as follows (Daugherty and Franzini, 1997):

$$z_1 + \frac{p_1}{\gamma} + \frac{\alpha_1 v_1^2}{2g} = z_2 + \frac{p_2}{\gamma} + \frac{\alpha_2 v_2^2}{2g} + h_f + h_j\,. \tag{4}$$

$Z_1 = L_0 + L_1$ and $Z_2 = L_0 + L_1 + L_2$ (see Fig. 1). The inlet water pressure $p_1 \neq 0$, and the outlet of water flow is free, $p_2 = 0$. In the test simulation, the flow velocity of the outlet can be measured under the conditions used to determine the seepage pressure. Thus, v_2 is known, and v_1 can be obtained by Eq. (2d). On the basis of Hagen–Poiseuille equation (Pisano, 2017), the frictional head loss along the pipe is as follows:

$$h_f = \frac{32L_0 \cdot \nu}{g \cdot d^2} v_1\,, \tag{5}$$

where d is the diameter of the circular tube. When $\alpha_1 = 1$ and $\alpha_2 = 1$, the following equation is obtained:

$$h_j = \frac{p_1}{\gamma} + \frac{v_1^2 - v_2^2}{2g} - L_2 - \frac{32L_0 \cdot \nu}{g \cdot d^2} v_1\,. \tag{6}$$

3. Experimental Setup

3.1 Specimens Preparation

The specimens are made of high-strength gypsum powder and water with a weight ratio of 4:1. The total weight of the specimen is 4.5 kg. At this moment, the colloidal liquidity of the specimen is relatively obvious. After the specimen is poured, it is condensed for 600–900 s, and demolding is conducted to enter the curing stage for 7 days. The specimens are placed in the laboratory to avoid external disturbance to ensure hardness and temperature uniformity.

The specimen shape is cylindrical, and the surface of the specimens is relatively smooth to minimize the roughness effect.

Table 2. Physical Properties of Gypsum Specimens

Density (kg/m^3)	Compressive strength (MPa)	Modulus of elasticity (MPa)	Poisson's ratio
1,790	47.82	2570	0.25

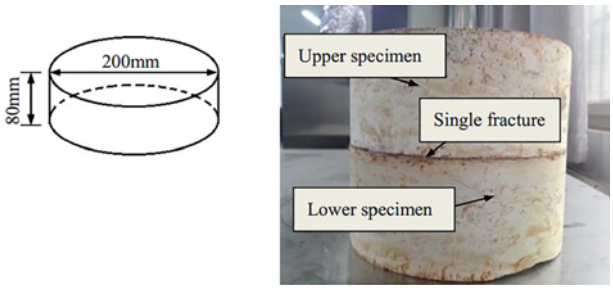

Fig. 2. Single Fracture of Gypsum Specimens

The physical parameters are shown in Table 2. Each group of tests consists of two specimens that overlap each other in the shearing box to form a single fracture (see Fig. 2). The seepage test adopts steady flow, and the water inlet is at the center of the lower specimen, which is fully penetrated. To reduce the local head loss of the water inlet, by referring to the experimental value of Esaki (1999) and comparing with Cao (2018), we selected the inlet diameter of the lower specimen to be 6 mm. No opening for a water inlet exists in the upper specimen. After the water passes through the hole, the internal radiation flow between the fractures is uniform. The outlet is equipped with a water collection measuring device, which can accurately measure the flow rate under different seepage pressures.

3.2 Test Sequence and Method

The test instrument adopts a TJXW–600 microcomputer-controlled system for coupling the direct shear and seepage of rock joints to apply normal force, shear force, and seepage

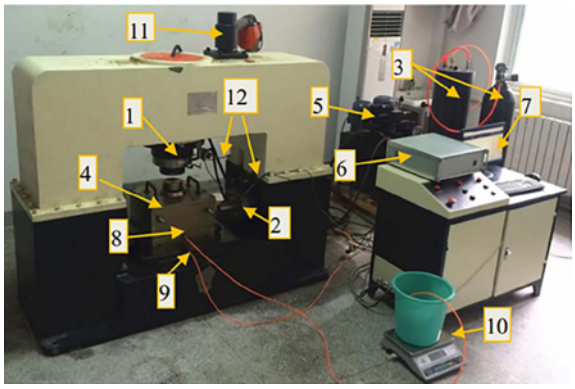

Fig. 3. Test Equipment System: (1) Normal-force Loading System, (2) Shear-force Loading System, (3) Hydraulic Pressure System, (4) Shear Box, (5) Hydraulic Servo Oil Source, (6) Closed-loop Monitoring Instrument, (7) Computer, (8) Water Inlet, (9) Water Outlet, (10) Water-collection Measuring Device, (11) Normal Load Controller, (12) Displacement Transducer

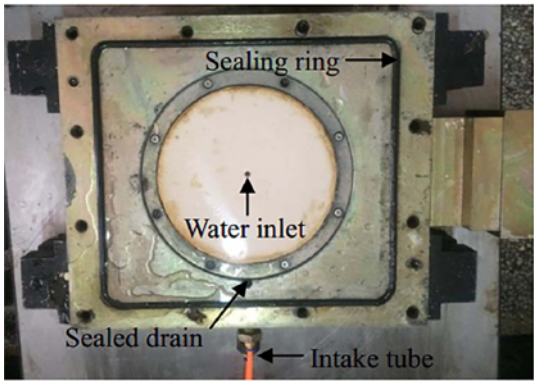

Fig. 4. Internal Structure of Lower Shear Box

Table 3. Test Conditions of Different Load Combinations

Cases	Normal force (kN)	Shear velocity (mm/s)	Seepage pressure (MPa)
Case 1	40	0.25	0.6
Case 2	50		0.6
Case 3	60		0.6
Case 4	70		0.6
Case 5	80		0.6
Case 6	60		0.2
Case 7	60		0.4
Case 8	60		0.8

pressure to the specimens. The shear box is well sealed; thus, the test system can constantly monitor the relationship between time and seepage, deformation, and force in all directions.

The sequence of load applied to the specimen is as follows. First, the normal force becomes stable when it is applied to the predetermined load. Second, seepage pressure is applied by the hydraulic pressure system. Finally, shear force is applied by the direct shear device after the numerical value of seepage pressure is stable. Fig. 3 shows the test equipment system diagram.

The lower shear box is fixed during the shear test. The internal structure of the lower shear box is presented in Fig. 4. The shearing friction between the specimen and the instrument is eliminated by the roller in the upper shear box, this reducing the test error. Consequently, the shearing contact between the upper and lower specimens is staggered. The instrument supplies 600 kN as the maximum shear force and normal force, and the seepage pressure is 3 MPa. The total shear displacement is 30 mm. The upper and lower specimens have a horizontal offset of 10 mm before the experiment begins. After the shearing test is complete, the upper specimen is biased to the other side by 20 mm. The applied seepage pressure is a fixed value. The load combination shown in Table 3 is used to simulate groundwater at a depth of 80–150 m below the surface (Cao *et al.*, 2018). Fig. 5 shows the external force of the shear box.

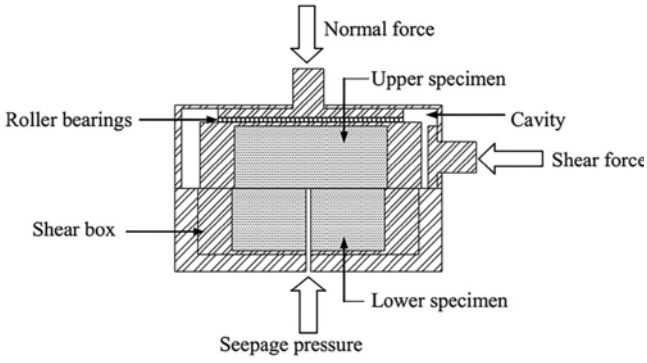

Fig. 5. External Force Diagram of the Shear Box

4. Test Results and Analysis

4.1 Specimen Destruction

After the test is complete, the surface of the lower specimen of Case 8 is destroyed. The scour damage range is approximately circular. The farthest deviation from the aperture is 10 mm. The maximum depth of damage is 4 mm. Traces of water flow, as well as gas holes and radiation damage, are observed on the lower surface of the upper specimen because gypsum is a non-hydraulic cementitious material. These phenomena are observed in Cases 1–8. The gas holes are approximately 1 mm in diameter. Several lines of water pattern exist along the flow direction. The upper surface of the lower specimen, where radiation occurs, is the same size as the water inlet (see Fig. 6). The lower specimen exerts a large flow effect at the orifice. The flow state is complicated, and the damage is localized. Similar results were also obtained by Dontsov (2016) and Peng (2016).

Experimental phenomena can be verified by theoretical calculations. The corresponding external force and local head loss can be obtained by substituting the seepage pressure and flow inlet velocity into Eqs. (3) and (6). When the seepage pressure is determined, the external force and energy loss are generally linear (see Fig. 7). When the seepage pressure is 0.8 MPa, the maximum external force is 1.389 kN compared with the vertical force, which is 1/60 to 1/30. The local head loss accounts for more than 95% of the total water head under each

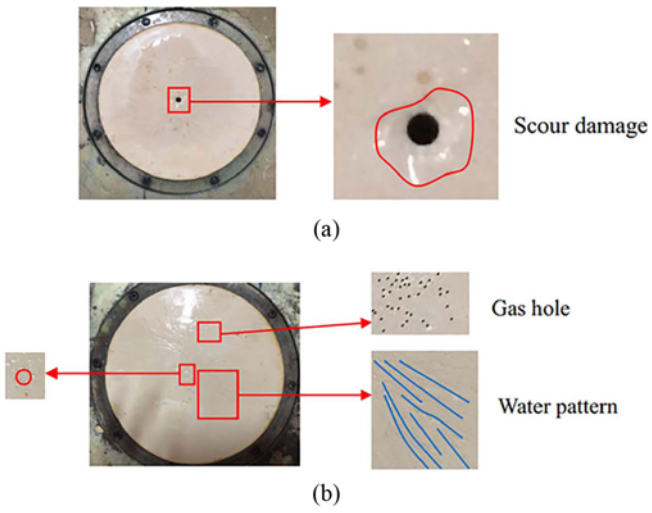

Fig. 6. Test Specimen Damage: (a) Bottom Surface of the Upper Specimen, (b) Upper Surface of the Lower Specimen

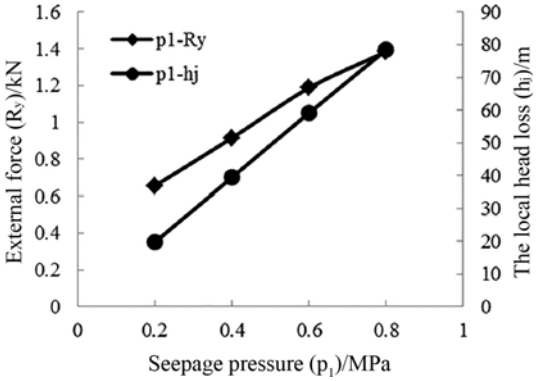

Fig. 7. Size of the Internal Force and Local Head Loss at Radiation Flow

seepage pressure; thus, the energy loss is the largest in the radiation area, and damage occurs easily. This finding is consistent with Fig. 6, and the damage occurs at the aperture of the radiation flow.

4.2 Mechanical Aperture Analysis

The application of external loads may cause changes in the size of fracture. The two specimens produce normal displacement due to the normal force. After an analysis was performed, it was revealed that the change in normal displacement was determined by two factors, namely, the fracture width and the normal deformation of specimen. The normal forces of 40, 50, 60, 70 and 80 kN are all in the elastic range. The final results are shown in Table 4. The strain of a gypsum specimen under each normal force can be obtained according to the elastic modulus and Poisson's ratio of the material. Normal stress can be calculated on the specimen surface. Deformation has a linear relationship with stress. For each 10 kN increase in the normal force, the specimen deformation increases by approximately 0.01 mm. The normal stress in the elastic range causes the specimen to be deformed at the 10^{-2} mm level.

In the test, normal force is applied to the specimen to form a mechanical aperture (Wang and Su, 2002). As the specimen in the preparation process, gypsum powder produces bubbles caused by water cooling. Consequently, the surface is not absolutely smooth and contains a few bumps. Each point on the surface of the two gypsum contacts is not fully exposed and belongs to the discrete phenomenon. Large fractures are selected as the main research object in the simulation, and the following assumptions are made.

Table 4. Strain Corresponding to Specific Normal Force

Normal force (kN)	Normal stress (MPa)	Strain (10^{-4})	Normal deformation (10^{-2} mm)
40	1.273	4.95	3.96
50	1.592	6.19	4.95
60	1.910	7.43	5.94
70	2.228	8.67	6.94
80	2.546	9.91	7.90

Table 5. Variations in Mechanical Aperture due to Specific Normal Force

Cases	Initial displacement (mm)	Final displacement (mm)	Total deformation (10^{-2} mm)	Change in mechanical aperture (mm)
Case 1	0	1.13	7.92	1.05
	0	1.71		1.63
Case 2	0	2.11	9.90	2.01
	0	1.63		1.53
Case 3	0	1.70	11.88	1.58
	0	2.32		2.20
Case 4	0	1.61	13.88	1.47
	0	1.58		1.44
Case 5	0	1.59	15.80	1.43
	0	1.97		1.81

1) The horizontal shear force exerts no effect on the normal displacement.
2) The normal deformation of the upper and lower specimens is equal.

Each group of tests is performed several times according to the different levels of normal force. The displacement during the test is recorded by a computer. In this paper, the normal downward displacement is defined as the positive direction. The variation distribution of the mechanical aperture is calculated. Two test results are selected for each working condition to reduce repetition, and they are summarized in Table 5.

As shown in Table 5, the initial and final displacements can be read by the computer. Each test includes two specimens; therefore, the total deformation is two times higher than that of the gypsum specimen. The change in the mechanical aperture is the difference between the normal displacement and the deformation of the upper and lower specimens.

When the normal force is the same, the error in the change in mechanical aperture between the two test results is 0.03–0.62 mm (Cases 4 and 3). The minimum and maximum deviations are 2% and 39%, respectively. The change in mechanical aperture tends to increase with the normal force. The variation in mechanical aperture increases by approximately 30% for every 10 kN increase in the normal force. However, when the normal force is 50 kN and 60 kN, a set of experimental results in which the change in mechanical aperture is more than 2 mm is obtained. This value is considerably larger than the normal force effect of 80 kN. This phenomenon is due to the presence of small bumps of varying heights on the gypsum surface. These bumps are subjected to vertical forces, which create stress concentrations that result in surface damage and debris production. Different sizes of debris cause different fracture sizes.

4.3 Comparison with Cubic Law

The change in mechanical aperture of each test is the final result. The amount of change in the mechanical aperture is assumed to be the fracture width (Esaki *et al*., 1999). Therefore, the effective corresponding seepage flow rate of each mechanical

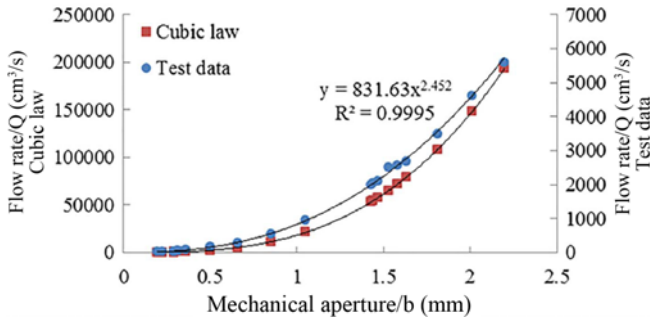

Fig. 8. Comparison between Experimental Results and Cubic Law

aperture according to all Cases is summarized in Fig. 8. From Fig. 8, a considerable difference exists between the test and cubic law theoretical data. The relationship between the test flow rate and mechanical aperture is simulated into the form of a power function as follows:

$$Q = m \cdot b^n , \tag{7}$$

where m and n are coefficients. Factors that affect the coefficient m include the seepage pressure, fracture width, unit weight of the fluid, and coefficient of viscosity.

After the analysis is performed, the final fitting result is obtained as follows:

$$Q = 831.63 \cdot b^{2.452} . \tag{8}$$

The flow rate is found by a power of 2.452 of mechanical aperture, and the fitting degree (R^2) is 0.9995. The fitting effect is good, and the relationship between the flow rate and mechanical aperture satisfies the power relation but belongs to the sub-cubic law. The reasons for the analysis are as follows. First, the specimen surface is not absolutely smooth. Second, the value of the seepage flow recorded in the test has a time error and therefore does not match the width of the mechanical aperture. Third, the flow rate is affected by shear and vertical forces.

4.4 Shear Behavior

In the horizontal direction, shear stress is affected by the normal force and seepage pressure. The effect is studied in Cases 1–8 by a single variable control law (see Fig. 9).

Case 3 is taken as an example. At the initial stage of shearing, the shear process can be divided into three stages. The A–B stage is called the elastic phase, and the shear stress has a linear relationship with time. Generally, a larger normal force indicates that the shear stress increases rapidly. The peak intensity is reached at point B. A positive correlation is identified between the shear peak strength and the normal force. When the normal force is 80 kN, the maximum shear stress sharply increases. The peak shear stress is 2.07 MPa, which is 35% higher than that of the other Cases. The B–C stage is called the yield phase. At this stage, the shear stress of Case 3 decreases. The decreasing trend is different due to the error in the sample preparation. The C–D stage enters the residual strength phase. When the shear process

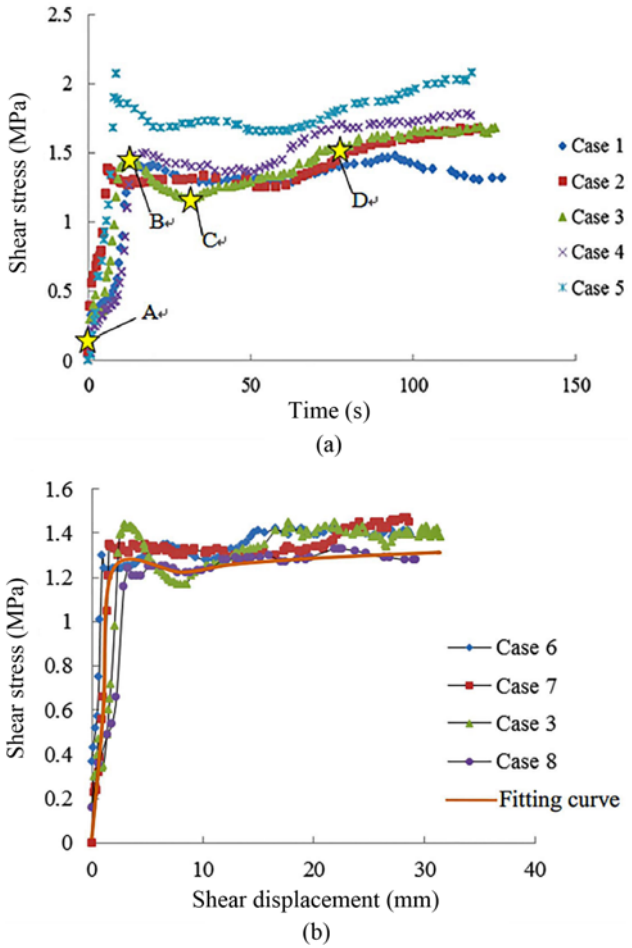

Fig. 9. Comparison of Shear Stress under All Cases: (a) Shear Stress Process of Different Normal Forces, (b) Shear Stress Process of Different Seepage Pressures

is stable, the shear stress change is minimal, although shear deformation continues. A large normal force indicates a great residual shear strength after stabilization. However, the specimen is in a balanced state due to constant shear movement. The trend and magnitude of the shear stress are similar under different seepage pressures. The common trend of the fitting curve is that in the initial phase of shearing, the displacement–stress is in the elastic phase, and the shear stress and deformation are linearly dependent. The shear displacement reaches approximately 5 mm, and the shear stress is approximately 1.3 MPa, thus reaching the peak strength and then entering a stable state. The fracture presents a shear swelling phenomenon because of the surface micro-convex body in the slippage process, and the intensity reaches its maximum. The effect of seepage pressure is less sensitive to shear stress than to normal force. Similar results were also obtained by Huang *et al.* (2002). The shear stress is related to the surface friction and up-slope angles.

5. Flow Velocity Simulation

The test data only show the macroscopic phenomena, such as

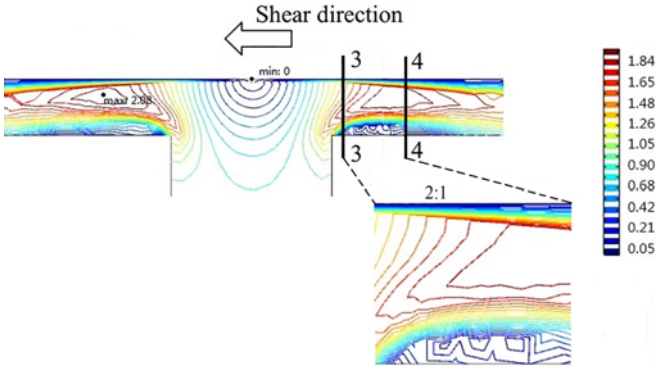

Fig. 10. Radiation Flow at Distribution of Numerical Simulation Contours (Unit: m/s)

flow rate and displacement. The microscopic phenomenon of the radiation flow between the fractures is unknown. Therefore, a finite element model should be established to supplement and improve the data.

The local analysis demonstrates that in the infinitesimal range, the volume of the water flow is considered to take up the same amount of space as the fracture. On the basis of Case 3, when the shear test is conducted at 40 s, the two specimens completely overlap. At this time, the fracture width is 2.20 mm, and the initial water flow velocity is 1,171 mm/s. Then, the current 2D fluid model is established (see Fig. 10). When the water flow comes into contact with the specimens, the normal velocity becomes 0 and the flow is along the horizontal direction. The outlet flow is governed by atmospheric pressure.

As shown in Fig. 10, the flow velocity is 0 when the flow is exposed to the upper specimen. When the flow changes to a horizontal orientation, the water flow in contact with the lower specimen presents a vortex phenomenon in the local range of 3–3 and 4–4. The *Re* value can reach 400,000, indicative of a turbulent state, and the water flow generates a vortex. The viscous force is greater than the inertial forces. Consequently, the pressure increases to create a pulsation, which can be destructive force on the lower specimen. At approximately 5 mm from the

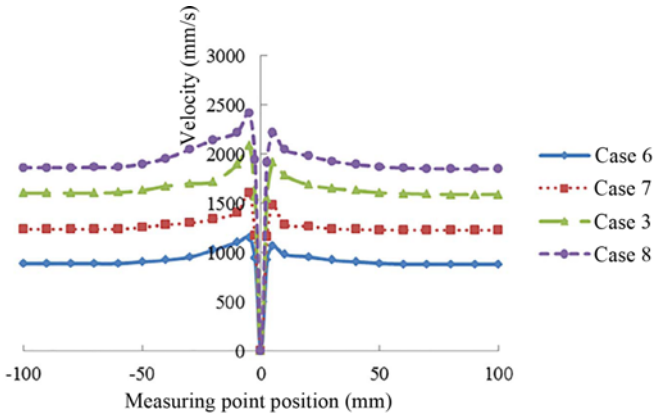

Fig. 11. Simulation of Fracture Surface Velocity under Different Seepage Pressures

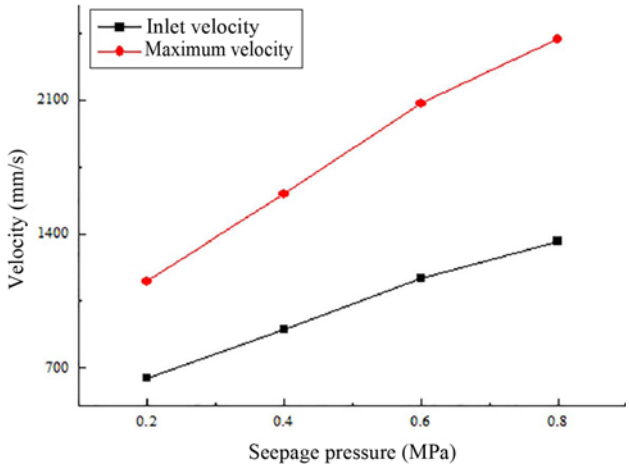

Fig. 12. Comparison Diagram of Inlet and Maximum Flow Velocity

radiation point, a maximum velocity point is determined at the same side of the shear direction, with a velocity of approximately 2080 mm/s, which is 1.78 times higher than that of the inlet velocity.

The water flow model with different seepage pressures is established by the same method (see Fig. 11). The point where radiation flow occurs between the fractures (the minimum flow velocity) is taken as the origin. The water flow to the right is defined as the positive X-axis direction. The shear direction is consistent with the opposite direction of the X-axis.

Different seepage pressures do not have an effect on the position of the radiation maximum flow velocity. The position of the maximum velocity is 5 mm to the left of the origin. The flow velocity on the same side as the shear direction is 8% higher than that on the other side. The flow velocity exhibits a non-Newtonian flow phenomenon because the water flow is under shear stress. In addition to the inertial force, the velocity is slightly high; thus, the seepage pressure is increased by 0.2 MPa, and the maximum flow velocity value is increased by approximately 450 mm/s. The flow velocity gradually decreased on both sides 5 mm away from the radiation flow. At approximately 50 mm on both sides, the velocity tends to be stable. The influence radius of radiation flow in this test is 50 mm. The area away from the radiation flow is in a laminar state.

The inlet and maximum velocities under different seepage pressures are compared to further verify the effect of the seepage pressure on the flow velocity. Fig. 12 shows that under the same seepage pressure, the maximum flow velocity is 78% higher than the inlet velocity. When the seepage pressure increases by 0.2 MPa, the difference between the maximum and inlet flow velocities is at least 500 mm/s and at most 1,050 mm/s. Therefore, the increase in seepage pressure is the most important factor causing damage to gypsum radiation flow.

6. Conclusions

The process of radiation flow among gypsum fractures is

studied by experiment and numerical simulation. The flow velocity distribution in the flow process is studied by applying different seepage pressures, and normal and shear forces. On the basis of the studied problem, the following findings are attained.

1. Gypsum specimens used in this test belong to an elastic material. On the basis of gypsum physical properties, the normal forces applied in the test satisfy the stress-strain relationship of gypsum. The normal displacement distribution measured by the instrument shows that the deformation of fracture width can reach 1,000 times the specimen deformation.
2. There is a large energy loss in the process of radiation flow, therefore, the relationship between flow rate and fracture width is different from cubic law. The flow and mechanical aperture measured by the test meet the sub-cubic law, and the best fitting relationship is $Q = 831.63 \cdot b^{2.452}$.
3. In the shearing process, the shear stress of gypsum is divided into the elastic phase, the yield phase and the residual strength phase, respectively. A positive correlation is identified between the shear peak strength and the normal force. In addition, the velocity of radial flow is greatly affected by shear stress. Numerical simulation analysis shows that the maximum velocity at the radiation flow along the shear direction is 1.78 times the inlet velocity.

These conclusions are applicable to the environment with low permeability and stable rock structure. Moreover, the relevant theory of radiation flow has been completed. However, these conclusions still need to be verified for deep underground water under the influence of complicated external forces. In addition, research on radiation flow will be meaningful for joints where the contact surface is a rough structure. Therefore, the next step is to apply the experimental results to practical engineering.

Acknowledgements

This work was supported by the program Shaanxi Provincial Key Innovative Research Team under Grant 2013KCT–15; the program Shaanxi Provincial Natural Science Foundation under Grant 2017JZ013; the program Hubei Provincial Key Laboratory Open Fund under Grant 2016KSD08; and the National Natural Science Foundation of China under Grant 51679197 and 51409208.

References

Adrian, R. J. (2006). "Structure of turbulent boundary layers." *Coherent Flow Structures at Earth's Surface*, J. G. Venditti, J. L. Best, M. Church, an R. J. Hardy, Eds., John Wiley & Sons, pp. 741-773.

Bai, B., He, Y., Li, X., Li, J., Huang, X., and Zhu, J. (2017). "Experimental and analytical study of the overall heat transfer coefficient of water flowing through a single fracture in a granite core." *Applied Thermal Engineering*, Vol. 116, pp. 79-90, DOI: 10.1016/ j.applthermaleng. 2017.01.020.

Cao, C., Xu, Z. G., Chai, J. R., Qin, Y., and Tan, R. (2018). "Mechanical and hydraulic behaviors in a single fracture with asperities crushed during shear." *International Journal of Geomechanics*, Vol. 18, No. 11, pp. 04018148-1–04018148-10, DOI: 10.1061/(ASCE) GM.1943-5622.0001277.

Chai, J. R. and Xu, W. S. (2011). "Coupling analysis of unsteady seepage and stress fields in discrete fractures network of rock mass in dam foundation." *Science China Technological Sciences*, Vol. 54, No. s1, pp. 133-139, DOI: 10.1007/s11431-011-4630-7.

Chamkha, A., Abbasbandy, S., and Rashad, A. M. (2015). "Non-Darcy natural convection flow for non-Newtonian nanofluid over cone saturated in porous medium with uniform heat and volume fraction fluxes." *International Journal of Numerical Methods for Heat & Fluid Flow*, Vol. 25, No. 2, pp. 422−437, DOI: 10.1108/HFF-02-2014-0027.

Coimbra, C. F. M. and Rangel, R. H. (2002). "General solution of the particle momentum equation in unsteady Stokes flows." *Journal of Fluid Mechanics*, Vol. 370, pp. 53-72, DOI: 10.1017/S0022112098001967.

Daugherty, R. L. and Franzini, J. B. (1977). "Fluid mechanics with engineering applications." 7th Edition. New York, NY: McGraw-Hill, pp. 192-564.

Develi, K. and Babadagli, T. (2015). "Experimental and visual analysis of single-phase flow through rough fracture replicas." *International Journal of Rock Mechanics & Mining Sciences*, Vol. 73, pp. 139-155, DOI: 10.1016/j.ijrmms.2014.11.002.

Dogonchi, A. S., Hatami, M., and Domairry, G. (2015). "Motion analysis of a spherical solid particle in plane Couette Newtonian fluid flow." *Powder Technology*, Vol. 274, pp. 186-192, DOI: 10.1016/j.powtec. 2015.01.018.

Dontsov, E. V. and Peirce, A. P. (2016). "A multiscale Implicit Level Set Algorithm (ILSA) to model hydraulic fracture propagation incorporating combined viscous, toughness, and leak-off asymptotics." *Computer Methods in Applied Mechanics & Engineering*, Vol. 313, pp. 53-84, DOI: 10.1016/j.cma.2016.09.017.

EI-Hakiem, M. A. (2000). "MHD oscillatory flow on free convection–radiation through a porous medium with constant suction velocity." *Journal of Magnetism & Magnetic Materials*, Vol. 220, Nos. 2-3, pp. 271-276, DOI: 10.1016/S0304-8853(00)00444-3.

Esaki, T., Du, S., Mitani, Y., Ikusada, K., and Jing, L. (1999). "Development of a shear-flow test apparatus and determination of coupled properties for a single rock joint." *International Journal of Rock Mechanics & Mining Sciences*, Vol. 36, No. 5, pp. 641-650, DOI: 10.1016/S0148-9062(99)00044-3.

Giwelli, A. A., Matsuki, K., Sakaguchi, K., and Kizaki, A. (2014). "Effects of non–uniform traction and specimen height in the direct shear test on stress and deformation in a rock fracture." *International Journal for Numerical & Analytical Methods in Geomechanics*, Vol. 37, No. 14, pp. 2186−2204, DOI: 10.1002/nag.2129.

He, G., Wang, E., and Liu, X. (2016). "Modified governing equation and numerical simulation of seepage flow in a single fracture with three-dimensional roughness." *Arabian Journal of Geosciences*, Vol. 9, No. 1, pp. 1-20, DOI: 10.1007/s12517-015-2036-8.

Huang, T. H., Chang, C. S., and Chao, C. Y. (2002). "Experimental and mathematical modeling for fracture of rock joint with regular asperities." *Engineering Fracture Mechanics*, Vol. 69, No. 17, pp. 1977-1996, DOI: 10.1016/S0013-7944(02)00072-3.

Jeong, W. C., Cho, Y. S., and Song, J. W. (2001). "A numerical study of fluid flow and solute transport in a variable-aperture fracture using geostatistical method." *KSCE Journal of Civil Engineering*, Vol. 5, No. 4, pp. 357-369, DOI: 10.1007/BF02829109.

Jin, Y., Dong, J., Zhang, X., Li, X., and Wu, Y. (2017). "Scale and size effects on fluid flow through self-affine rough fractures." *International*

Journal of Heat & Mass Transfer, Vol. 105, pp. 443-451, DOI: 10.1016/j.ijheatmasstransfer.2016.10.010.

Kang, S. and Sotiropoulos, F. (2015). "Large-eddy simulation of three-dimensional turbulent free surface flow past a complex stream restoration structure." *Journal of Hydraulic Engineering,* Vol. 141, No. 10, DOI: 10.1061/(ASCE)HY.1943-7900.0001034.

Li, B., Liu, R., and Jiang, Y. (2016). "Influences of hydraulic gradient, surface roughness, intersecting angle, and scale effect on nonlinear flow behavior at single fracture intersections." *Journal of Hydrology*, Vol. 538, pp. 440-453, DOI: 10.1016/j.jhydrol.2016.04.053.

Liu, R., Jiang, Y., and Li, B. (2016). "Effects of intersection and dead-end of fractures on nonlinear flow and particle transport in rock fracture networks." *Geosciences Journal*, Vol. 20, No. 3, pp. 415-426, DOI: 10.1007/s12303-015-0057-7.

Ma, X., Tian, M., Zhang, J., Tang, L., and Liu, F. (2018). "Flow pattern identification for two-phase flow in a U-bend and its contiguous straight tubes." *Experimental Thermal & Fluid Science*, Vol. 93, pp. 218-234, DOI: 10.1016/j.expthermflusci.2017.12.024.

McClure, M. W., and Kang, C. A. (2017). "A three-dimensional reservoir, wellbore, and hydraulic fracturing simulator that is compositional and thermal, tracks proppant and water solute transport, includes non-darcy and non-newtonian flow, and Handles fracture closure." *SPE Reservoir Simulation Conference. Society of Petroleum Engineers*, Montgomery, TX. USA, DOI: 10.2118/182593-MS.

Nguyen-Thoi, T., Phung-Van, P., Ho-Huu, V., and Le-Anh, L. (2015). "An Edge-based Smoothed Finite Element Method (ES-FEM) for dynamic analysis of 2D fluid-solid interaction problems." *KSCE Journal of Civil Engineering*, Vol. 19, No. 3, pp. 641-650, DOI: 10.1007/s12205-015-0293-4.

Oda, M., Takemura, T., and Aoki, T. (2002). "Damage growth and permeability change in triaxial compression tests of Inada granite." *Mechanics of Materials*, Vol. 34, No. 6, pp. 313-331, DOI: 10.1016/S0167-6636(02)00115-1.

Peng, Y., Li, Y., and Zhao, J. (2016). "A novel approach to simulate the stress and displacement fields induced by hydraulic fractures under arbitrarily distributed inner pressure." *Journal of Natural Gas Science & Engineering*, Vol. 35, pp. 1079-1087, DOI: 10.1016/j.jngse.2016.09.054.

Pisano, A. (2017). "From tubes and catheters to the basis of hemodynamics: The Hagen–Poiseuille equation." *Physics for Anesthesiologists*, pp. 55-61, DOI: 10.1007/978-3-319-57330-4_7.

Qian, J., Zhan, H., Zhao, W., and Sun, F. (2005). "Experimental study of turbulent unconfined groundwater flow in a single fracture." *Journal of Hydrology*, Vol. 311, Nos. 1-4, pp. 134-142, DOI: 10.1016/j.jhydrol.2005.01.013.

Raptis, A. (1998). "Radiation and free convection flow through a porous medium." *International Communications in Heat & Mass Transfer*, Vol. 25, No. 2, pp. 289-295, DOI: 10.1016/S0735-1933(98)00016-5.

Rashidi, M. M., Bagheri, S., Momoniat, E., and Freidoonimehr, N. (2015). "Entropy analysis of convective MHD flow of third grade non-Newtonian fluid over a stretching sheet." *Ain Shams Engineering Journal*, Vol. 8, No. 1, pp. 77-85, DOI: 10.1016/j.asej.2015.08.012.

Rong, G., Hou, D., Yang, J., Cheng, L., and Zhou, C. (2017). "Experimental study of flow characteristics in non-mated rock fractures considering 3D definition of fracture surfaces." *Engineering Geology*, Vol. 220, pp. 152-163, DOI: 10.1016/j.enggeo.2017.02.005.

Seo, H., Kang, T., Felix, M. L., and Lee, S. (2017). "A study to determine the location of perforated drainpipe in a levee for controlling the seepage line." *KSCE Journal of Civil Engineering*, Vol. 22, No. 1, pp. 153-160, DOI: 10.1007/s12205-017-1330-2.

Sheikholeslami, M., Ganji, D. D., Javed, M. Y., and Ellahi, R. (2015). "Effect of thermal radiation on magnetohydrodynamics nanofluid flow and heat transfer by means of two phase model." *Journal of Magnetism & Magnetic Materials*, Vol. 374, pp. 36-43, DOI: 10.1016/j.jmmm.2014.08.021.

Subbarao, A., Prasad, V. R., Nagendra, N., Reddy, N. B., and Beg, O. A. (2016). "Non-similar computational solution for boundary layer flows of non-newtonian fluid from an inclined plate with thermal slip." *Journal of Applied Fluid Mechanics*, Vol. 9, No. 2, pp. 795-807, DOI: 10.18869/acadpub.jafm.68.225.24664.

Tang, Z. C., Xia, C. C., Jiao, Y. Y., and Wong, L. N. Y. (2016). "Closure model with asperity interaction in normal contact for rock joint." *International Journal of Rock Mechanics & Mining Sciences*, Vol. 83, pp. 170-173, DOI: 10.1016/j.ijrmms.2015.12.006.

Wang, Y. and Su, B. Y. (2002). "Research on the behavior of fluid flow in a single fracture and its equivalent hydraulic aperture." *Advances in Water Science*, Vol. 13, No. 1, pp. 61-68.

Witherspoon, P. A., Wang, J. S. Y., Iwai, K., and Gale, J. E. (1979). "Validity of Cubic Law for fluid flow in a deformable rock fracture." *Water Resources Research*, Vol. 16, No. 6, pp. 1016-1024, DOI: 10.1029/WR016i006p01016.

Xia, C. C., Qian, X., Lin, P., Xiao, W. M., and Gui, Y. (2016). "Experimental investigation of nonlinear flow characteristics of real rock joints under different contact conditions." *Journal of Hydraulic Engineering*, Vol. 143, No. 3, pp. 04016090-1–04016090-14, DOI: 10.1061/(ASCE)HY.1943-7900. 0001238.

Xu, J., Xie, X., Yang, C., and Shen, Z. (2017). "Test and analysis of hydraulic fracture characteristics of rock single crack." *Fluid Mechanics*, Vol. 4, No. 3, DOI: 10.4172/2476-2296.1000164.

Yun, W. C., Dong, H. S., Cho, S. E., Im, E. S., and Kim, D. S. (2013). "Seepage behavior of drainage zoning in a concrete faced gravel-fill dam via centrifuge and numerical modeling." *KSCE Journal of Civil Engineering*, Vol. 17, No. 5, pp. 949-958, DOI: 10.1007/s12205-013-0215-2.

Zhang, C., Zhang, Y., Li, Z., Zhang, T., Liu, T., and Xie, Y. (2016). "Experimental study of seepage characteristics of single rock fracture based on stress states and stress history." *Global Geology*, Vol. 19, No. 3, pp. 177-181, DOI: 10. 3969 /j. issn.1673-9736.2016.03.06.

Zhao, Y., Zhang, L., Wang, W., Tang, J., Lin, H., and Wan, W. (2017). "Transient pulse test and morphological analysis of single rock fractures." *International Journal of Rock Mechanics & Mining Sciences*, Vol. 91, pp. 139-154, DOI: 10.1016/j.ijrmms.2016.11.016.

Zou, L., Jing, L., and Cvetkovic, V. (2017). "Shear-enhanced nonlinear flow in rough-walled rock fractures." *International Journal of Rock Mechanics & Mining Sciences*, Vol. 97, pp. 33-45, DOI: 10.1016/j.ijrmms.2017.06.001.